Numerical simulation of homojunction *p-i-n* $In_{0.4}Ga_{0.6}N$ solar cell with different absorber layer configurations

A.K. Tan[a], H.U. Manzoor[b, c], N.A. Hamzah[a], M.A. Ahmad[a], S.S. Ng[a, *], Z. Hassan[a]

[a]*Institute of Nano Optoelectronics Research and Technology (INOR), Universiti Sains Malaysia, 11800 USM, Penang, Malaysia.*

[b]*School of Engineering, University of Glasgow, Glasgow G12 8QQ, Scotland, United Kingdom.*

[c]*University of Engineering and Technology, Lahore-FSD Campus, 38000, Pakistan.*

**Corresponding author: shashiong@usm.my*

ABSTRACT:

The effects of thickness, carrier densities, and absorber layer (*p*-In0.4Ga0.6N) configurations were evaluated. Numerical studies were performed to optimize the homojunction *p-i-n* $In_{0.4}Ga_{0.6}N$ solar cell using SCAPS-1D. With the optimized thicknesses and carrier densities, the *p-i-n* $In_{0.4}Ga_{0.6}N$ solar cell shows a maximum conversion efficiency of 18.74%. By changing the fixed indium composition of the absorber layer into step- and linear-graded configurations, the conversion efficiency, open-circuit voltage, and short-circuit current density of the solar cell were further improved. The results showed that the solar cells with step- and linear-graded absorbers attained maximum conversion efficiency of 19.77% and 19.84%, respectively. These results implied that the absorber with the graded compositional design helps to reduce the barrier height of electron-hole transport for band-to-band and inter-band absorption. This eventually reduces the energy loss caused by phonon emission and heat thermalization.

Keywords: III-V nitride, InGaN, thin-film solar cell, homojunction, photovoltaic

Highlights

- Optimization of intermediate indium composition *p-i-n* homojunction solar cell by using SCAPS-1D
- Implementation of novel step-graded and linear-graded absorber layer to improve the performance of the solar cell
- Achieved quantum efficiency (QE) close to 100% by using novel absorber configurations.
- Reduction of photon energy losses through thermalization and phonon emission with graded absorber system configurations.
- Aware of the potential of intermediate indium composition InGaN-based solar cells in the market.

1. Introduction

Various photovoltaic (PV) technologies have been developed to mitigate the reliability of fossil fuels in producing electricity. Such PV technologies are crystalline silicon, cadmium telluride (CdTe), copper indium gallium selenide (GICS), perovskite, organic, multijunction III-V, and dye-sensitized solar cell (DSSC) [1]. However, most of these technologies are susceptible to ionized electrons produced by radiation which will act as stable impurity complexes to alter the optical, electrical, and structural properties of the solar array [2–4]. Therefore, material such as indium gallium nitride (InGaN) has gained attention due to its extraordinary properties. InGaN is a promising material for optoelectronic devices such as solar cells, laser diodes, light-emitting diodes, and high electron mobility transistors. This is mainly attributed to its tunable direct bandgap energy characteristics from 0.70 eV (infrared) to 3.42 eV (ultraviolet) by varying the indium (In) composition. Thus, InGaN is an excellent candidate for solar cell application since it can cover almost the entire spectrum from solar irradiation [5]. The incorporation of indium nitride (InN) improved the radiation resistance of InGaN when subjected to proton irradiation, which dominates the radiation environment in space. Eventually, InGaN has a longer carrier lifetime when compared to gallium arsenide (GaAs) and indium gallium arsenide (InGaAs), which makes it a promising solar cell material for space exploration [6].

Typically, for the InGaN-based single-junction solar cell to achieve a conversion efficiency of more than 20%, InGaN layers with an indium composition of more than 40% and several hundred nanometers are required [7–10]. However, the growth of thick and high-quality In-rich InGaN (i.e., with In composition of more than 40%) is extremely challenging due to several constraints such as high equilibrium nitrogen (N) vapor pressure, low dissociation temperature of InN (around 650 °C), difficulty to obtain lattice-matched substrate, and the thermodynamic stability [11]. Besides that, thick In-rich InGaN thin films often encountered

phase separation and compositional fluctuation due to the miscibility gap between InN and GaN species [12]. The presence of compositional fluctuation and other defects within the thin film is detrimental to the open-circuit voltage (V_{oc}) and short circuit current density (J_{sc}) of the In-rich InGaN-based solar cell [13]. Hence, InGaN layers with intermediate In composition is favorable for the solar cell application.

Islam *et al*. (2013) have successfully grown thick InGaN thin film with intermediate In composition (~40%) using metal-organic vapor phase epitaxy. X-ray diffraction profile (2θ-ω) showed no phase separation, indicating good compositional homogeneity of the InGaN thin film. Their study also showed that the thermal expansion coefficient mismatch between the GaN template and In-rich InGaN was the root cause of the film quality deterioration. The dislocations were introduced to achieve strain relaxation during the growth [14]. Guo *et al.* (2010) optimized the growth conditions of InGaN by varying growth temperature, V/III ratio, and trimethylindium/ (trimethylindium + triethylgallium) ratio. Although the studies showed the maximum In incorporation up to 100%, phase separations were observed for InGaN thin films with In composition above 60% due to thermodynamic instability. They managed to grow single-phase InGaN samples with In composition between 10% to 45% [15]. Sang *et al.* (2021) reported the growth of $In_{0.4}Ga_{0.6}N$ with a thickness of more than 300 nm by using high pressure MOCVD with the growing pressure up to 2.5 atm, and the growth temperature varied from 680-830 °C. It was found that high pressure growing conditions could improve the crystalline quality and better surface morphology of the InGaN thin film. Phase separation in the In-rich InGaN thin was suppressed under high-pressure growing conditions [16]. Hence, the growth of intermediate In composition InGaN (~40%) can be assumed to be consistent based on the current advances. Apart from that, the growth of In-rich *p*-type InGaN thin film is another challenge for developing In-rich InGaN solar cells. Several studies found that the magnesium (Mg) dopant flow rate, growth temperature, and annealing temperatures play important roles

in forming *p*-InGaN [11]. Heavy Mg doping concentration deteriorates the crystalline quality of the *p*-InGaN by phase separation [17]; while *n*-type electrical characteristic increases due to electron accumulation on the surface of the thin film in *p*-type InGaN with increasing In composition [18]. Therefore, the p-InGaN is limited to having In composition of less than 40% and a maximum hole concentration of around 10^{19} cm^{-3} [11,19–21]. Hence, the growth of InGaN solar cells with intermediate In composition (~40%) is feasible with the current growth advances.

From literature reviews, several growth challenges of In-rich InGaN were pinpointed. Those challenges limit the growth stability of the In-rich InGaN with In composition of more than 30% and hole concentration of more than 10^{19} cm^{-3}. Next, the GaN/InGaN heterostructure not only introduces more dislocation into the thin films but also induces piezoelectric polarization, which will create drift currents opposite in direction to reduce the carrier collection efficiency [22]. In this work, we studied a three-layered *p-i-n* homojunction solar cell with intermediate indium composition of 40%, which used the current growth limitations to evaluate the performance of the InGaN solar cell. The homojunction *p-i-n* was proposed to minimize the effect of piezoelectric polarization and the lattice mismatch issue in the solar cell structure. The carrier density investigation was carried out to pinpoint the best carrier densities required to achieve maximum conversion efficiency. Several studies showed that the defect and dislocation densities are the main reason limiting the performance of InGaN *p-i-n* solar cells [23,24]. Therefore, the effect of dislocation densities was taken into consideration.

In this paper, the optimization of standard *p-i-n* $In_{0.4}Ga_{0.6}N$ has been done by varying the thickness and carrier density. To further improve the solar cell performance, novel step- and linear-graded absorber designs were proposed. The simulation data for standard, step- and linear-graded $In_{0.4}Ga_{0.6}N$ were compared to identify the best graded absorber configuration.

2. Theoretical modeling and simulation

In this paper, three different solar cell structures were investigated, and their respective configurations are shown in Figure 1. The first one is named standard *p-i-n* layer structure, utilizing a fixed absorber layer of $In_{0.4}Ga_{0.6}N$ material. The second and third are linear- and step-graded absorber structures using graded $In_xGa_{1-x}N$ absorber layers. The configured absorber layers were proposed using the optimized structure of the standard *p-i-n*. All the simulations were performed using the SCAPS-1D solar cell simulator developed by the University of Gent, Belgium.

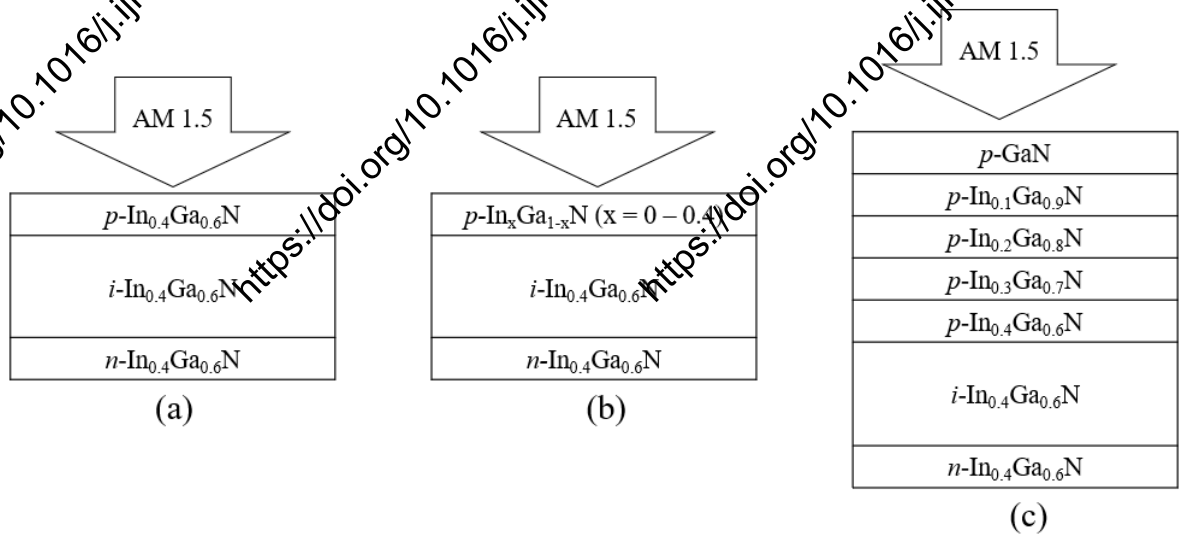

Figure 1. Schematic diagrams of InGaN solar cells with different configurations: (a) standard, (b) linear-graded absorber, and (c) step-graded absorber *p-i-n* solar cell structures.

In this study, the bandgap energy, E_g of the $In_xGa_{1-x}N$ can be estimated by using the Vegard law, as expressed in Eq. (1)

$$E_g(In_xGa_{1-x}N) = x.E_g^{InN} + (1-x)E_g^{GaN} - b.x.(1-x) \quad (1)$$

where x is the In composition of the $In_xGa_{1-x}N$; E_g^{InN} is the bandgap energy of indium nitride (InN) and is equal to 0.70 eV; E_g^{GaN} is the bandgap energy of gallium nitride (GaN) and is equal to 3.42 eV; b is the bowing factor equal to 1.43 eV. The electron and hole mobilities can be calculated as a function of carrier density with the Caughey-Thomas approximation [10], as shown in Eq. (2)

$$\mu_i(N) = \mu_{min,i} + \frac{\mu_{max,i} - \mu_{min,i}}{1+\left(\frac{N}{N_{ref}}\right)^{\gamma_i}}, \quad (2)$$

where i represents either electrons (e) or holes (h); N represents the carrier density; μ_{min} and μ_{max} represent the minimum and maximum mobilities of III-V nitride; γ is the specific parameter for InN and GaN, and N_{ref} is the reference carrier density of 1×10^{17} cm^{-3}. The mobilities of the InGaN can be calculated using Eq. (2). The parameters used to calculate the mobilities of the InGaN are summarized in Table 1.

Table 1. Parameters used to calculate the mobilities of the InGaN

	$\mu_{min,e}$ (cm^2/Vs)	$\mu_{max,e}$ (cm^2/Vs)	γ_e	$\mu_{min,h}$ (cm^2/Vs)	$\mu_{max,h}$ (cm^2/Vs)	γ_h	Ref.
InN	429	3970	1	20	220	2	[25,26]
GaN	55	1000	1	3	170	2	[27]

The dielectric permittivity (ε) and the electron affinity (χ) of $In_xGa_{1-x}N$ can be expressed using Eqs. (3) and (4), respectively [28]:

$$\varepsilon(In_xGa_{1-x}N) = 15.3x + 8.9(1-x) \quad (3)$$

$$\chi(In_xGa_{1-x}N) = 4.1 + 0.7(3.42 - E_g) \quad (4)$$

The effective density state of conduction (N_c) and the valence band (N_v) of the $In_xGa_{1-x}N$ can be expressed using Eqs. (5) and (6), respectively;

$$N_c = \big(0.9x + 2.3(1-x)\big) \times 10^{18} \tag{5}$$

$$N_v = \big(5.3x + 1.8(1-x)\big) \times 10^{19} \tag{6}$$

The absorption coefficients of $In_xGa_{1-x}N$ can be expressed as wavelength-dependent parameters as defined in Eq (7):

$$\alpha(E_g) = \alpha_o \sqrt{\frac{E - E_g(x)}{E_g(x)}} \tag{7}$$

where $E_g(x)$ is the bandgap energy of $In_xGa_{1-x}N$, E is the photon energy of wavelengths and α_o is the reference absorption coefficient. The absorption coefficient of InGaN is assumed to be the same as GaN, which is approximately 2×10^5 cm^{-1} [29].

This study performed the simulations at 300 K with an incident solar radiation of 1000 W/m^2 (AM 1.5G) as the environmental boundary conditions. Table 2 shows the initial boundary conditions and the parameters used to evaluate the performance of the standard *p-i-n* InGaN solar cell. The optimizations were first performed on the standard *p-i-n* structure by varying the thickness of *p-, i-*, and *n*-layers consecutively to obtain the optimized thickness of each layer. Next, the carrier density of each layer was varied from 10^{13} cm^{-3} to 10^{21} cm^{-3} to study the effect of carrier density on the solar cell's overall efficiency. Subsequently, the solar cell performance of standard *p-i-n* was compared with the configured absorber structures (e.g., linear graded *p-i-n* and step graded *p-i-n*) to investigate the roles of tunnel absorber structure in the performance of the InGaN solar cell. Several experimental results indicated that the

defect density of the InGaN thin film is within 10^{10} - 10^{12} cm^{-3} [30,31], to consider the possible occurrence of the defect during the fabrication processes, the defect density, N_t has been increased by two orders of 10^{14} cm^{-3} for this study.

Table 2. Initial boundary conditions and the parameters used for evaluating the *p-i-n* InGaN-based solar cell.

Structural parameters	Values
p-layer initial thickness	25 nm
i-layer initial thickness	100 nm
n-layer initial thickness	100 nm
Acceptor doping density in *p*-layer, N_A	1×10^{18} cm^{-3}
Carrier density of intrinsic layer, $N_D = N_A$	1×10^{16} cm^{-3} [31]
Donor doping density in *n*-layer, N_D	1×10^{18} cm^{-3}
Pre-existing defect density, N_t	1×10^{14} cm^{-3}
Radiative recombination coefficient, B	9.6×10^{-10} cm^3 s^{-1} [32]
Auger electron and hole capture coefficient, C_p and C_n	1.7×10^{-31} cm^6/s [33]

3. Results and discussion

3.1 Optimization of Standard *p*-$In_{0.4}Ga_{0.6}N$/ *i*-$In_{0.4}Ga_{0.6}N$/ *n*-$In_{0.4}Ga_{0.6}N$

The optimization of the InGaN solar cell was started by varying the absorber's thickness from 25 nm to 500 nm; the extracted simulation results are shown in Figures 2(a) and 2(b). Under initial boundary conditions, the fill factors (*FF*), conversion efficiency (η), short circuit current density (J_{sc}), and open-circuit voltage (V_{oc}) are 90.42%, 15.33%, 11.29 mA/cm^2, and 1.50 V, respectively. The η of the solar cell increases up to 16.68% at an absorber thickness of 150 nm. Beyond 150 nm, the η was reduced to 13.50% at the thickness of 500 nm. The V_{oc} and J_{sc} also showed a similar trend as the η. In contrast, the *FF* increased with the absorber thickness. As the absorber thickness gradually increased to 150 nm, more electron-hole pairs were generated, leading to a higher radiative recombination rate and forward bias diffusion current, *J*. As the absorber layer thickness exceeded the critical thickness (~150 nm), the η was reduced due to the reduction of the electric field [34] to separate electron-hole pairs. The reduction of radiative

recombination reduces the short-circuit current density, J_{sc}. The relations of V_{oc} with J_{sc} and J_o of the solar cell are described in Eq. (8).

$$V_{oc} = \frac{kT}{q} ln \left[\frac{J_{sc}}{J_o} + 1\right], \tag{8}$$

where $\frac{kT}{q}$ is the thermal voltage and J_o is the saturation current density. Next, the *FF* is inversely proportional to the J_{sc} and V_{oc}. It increases with the increment of the absorber thickness, which also indicates the reduction of series resistance and less power loss due to heat dissipation.

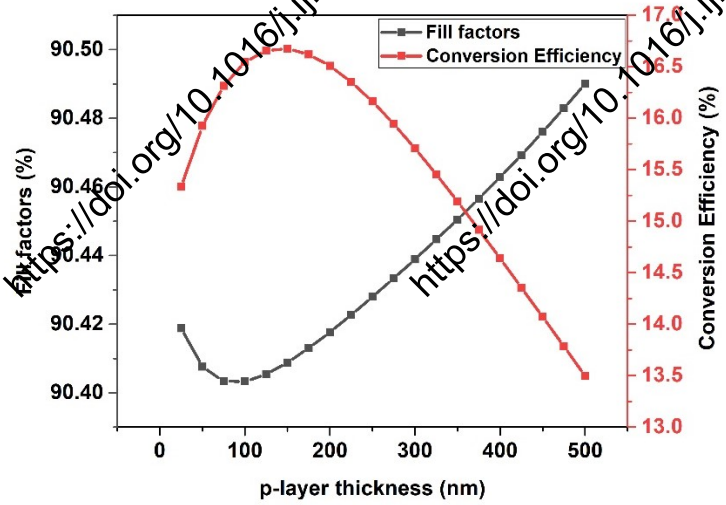

(a)

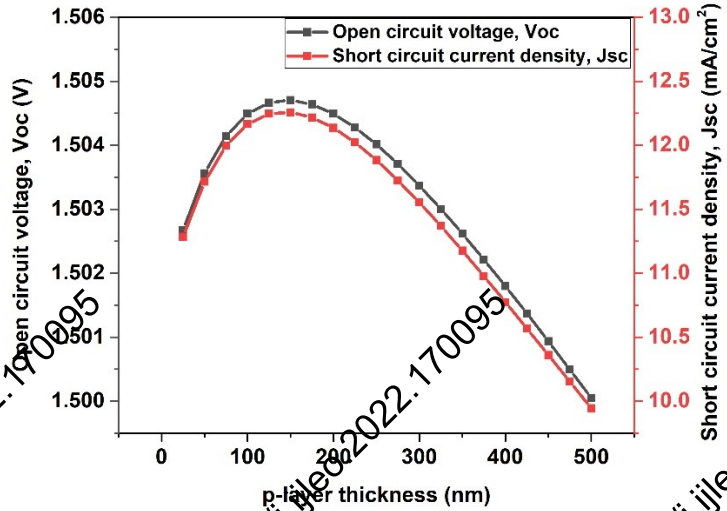

(b)

Figure 2. Effects of absorber's (*p*-layer) thickness on (a) fill factors and conversion efficiency, and (b) open circuit voltage and short circuit current density of *p-i-n* InGaN-based solar cell.

Figures 3(a) and 3(b) show the effects of *i*-layer thickness on *FF*, J_{sc}, V_{oc}, and η of *p-i-n* InGaN-based solar cells. The thickness of the intrinsic (*i*-) layer varied from 25 nm to 1000 nm. As the thickness of the *i*-layer increases to 675 nm, the maximum η of 18.44% was achieved. The *FF*, V_{oc}, and J_{sc} of the optimized *i*-layer thickness are 90.91%, 1.50 V, and 13.55 mA/cm^2, respectively. There is no significant change to the η after 675 nm. In comparison, *FF* shows a slight fluctuation of 0.14% (i.e., from 90.91% at 675 nm to 90.78% at 1000 nm). J_{sc} and V_{oc} demonstrated the opposite trend. The V_{oc} reduced while the J_{sc} increased with the intrinsic layer thickness, as shown in Figure 3(b). As the thickness of the *i*-layer increases, more photons will be absorbed to generate electron-hole pairs due to widening the depletion region and contributing to the improvement of J_{sc}. The wide depletion region elongated the ion diffusion length. Hence, the carriers' lifetime and the drift current density will increase [35]. The opposite trends of J_{sc} and V_{oc} of the *p-i-n* solar cell can be explained by the J_o increment across the *i*-layer thickness by the Sah-Noyce-Shockley approximation [36], as expressed in Eq. (9).

$$J_o = \frac{qn_iW}{\sqrt{\tau_e\tau_h}}, \tag{9}$$

where q is the elementary charge, n_i is the intrinsic carrier concentration, W is the width of the depletion zone, τ_e and τ_h are respectively, the electron and the hole lifetimes. A wider *i*-layer thickness contributed to a wider depletion zone, eventually increasing the saturation current density, J_o. Hence, the V_{oc} is predicted to be lowered as the thickness of the *i*-layer increases, as shown in Figure 3(b).

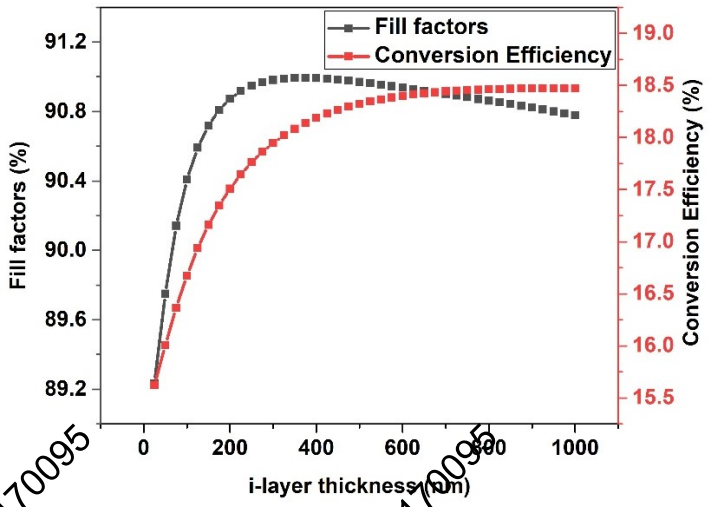

(a)

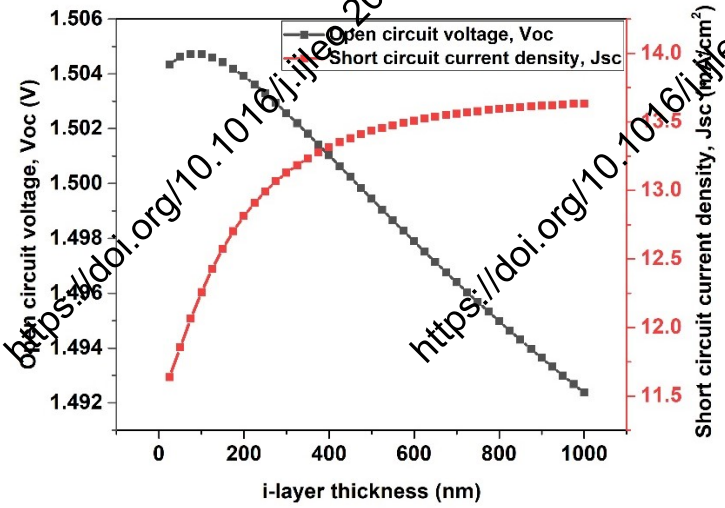

(b)

Figure 3. Effects of i-layer thickness on (a) fill factors and conversion efficiency, and (b) open circuit voltage and short circuit current density of p-i-n InGaN-based solar cell.

Figures 4(a) and (b) show the effects of the donor (n) layer's thickness on FF, J_{sc}, V_{oc}, and η. As the thickness of the n-layer increases from 25 nm to 350 nm, the η of the solar cell increases from 13.40% to 18.48%. Beyond 350 nm, there are no changes to the η and FF. The J_{sc} and V_{oc} demonstrated the same trend. These values increased and remained constant after a certain n-layer thickness. It can be concluded that the n-layer is less susceptible to thickness changes after reaching the critical thickness (~350 nm). Figure 4(a) shows that the values of

the *FF* converge at 90.87% after exceeding 300 nm of *n*-layer thickness. It can be explained by the correlation of maximum output power (P_{max}), V_{oc}, and J_{sc}, as expressed in Eq. (10).

$$Fill\ factor\ (FF) = \frac{P_{max}}{V_{oc} \times J_{sc}}, \tag{10}$$

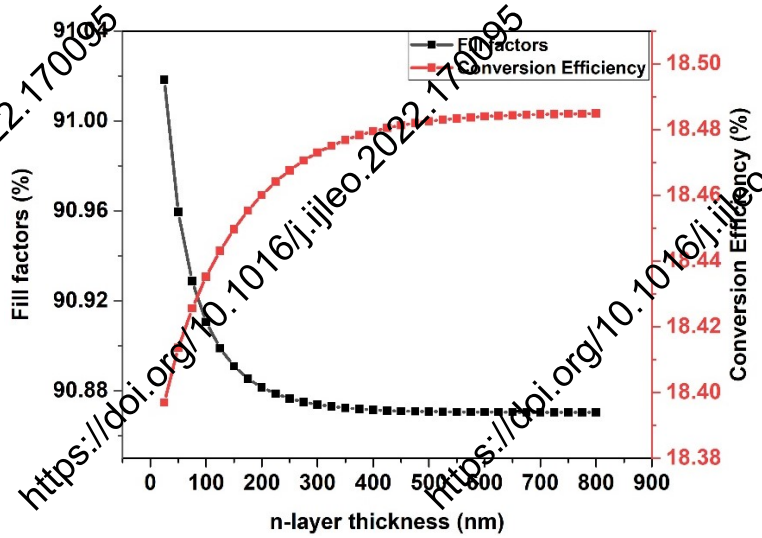

(a)

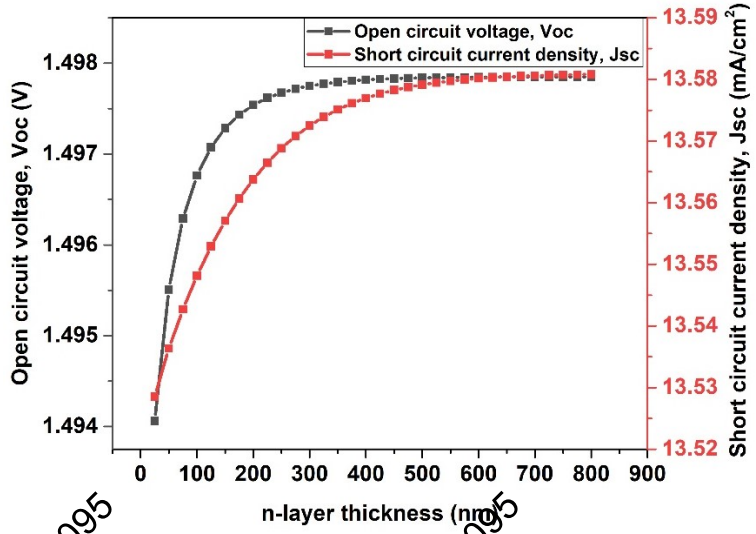

(b)

Figure 4. Effects of *n*-layer's thickness on (a) fill factors and conversion efficiency, (b) open circuit voltage and short circuit current density of *p-i-n* InGaN-based solar cell.

As the thickness of the *n*-layer increased, the V_{oc} and J_{sc} also increased and remained constant across subsequent thicknesses. Hence, the *FF* of the solar cell also became constant across the thicker *n*-layer. In summary, the optimized thickness for the *p*-$In_{0.4}Ga_{0.6}N$/ *i*-$In_{0.4}Ga_{0.6}N$/ *n*-$In_{0.4}Ga_{0.6}N$ solar cell is 150 nm/ 675 nm/ 350 nm. The *FF*, η, J_{sc}, and V_{oc} for this optimized structure are 90.87%, 18.48%, 13.58 mA/cm^2, and 1.50 V, respectively.

3.2 Effect of carrier densities to standard *p*-$In_{0.4}Ga_{0.6}N$/ *i*-$In_{0.4}Ga_{0.6}N$/ *n*-$In_{0.4}Ga_{0.6}N$

The optimized *p*-$In_{0.4}Ga_{0.6}N$/ *i*-$In_{0.4}Ga_{0.6}N$/ *n*-$In_{0.4}Ga_{0.6}N$ solar cell structure obtained from section 3.1 will be used to evaluate the effect of carrier density on the performance of the solar cell. The carrier density of each layer varied from 1×10^{13} cm^{-3} to 1×10^{21} cm^{-3}. The carrier mobilities of the $In_{0.4}Ga_{0.6}N$ were recalculated by using Eq. (2). Other parameters remain at their respective initial values.

Figures 5(a) and (b) show the effects of absorber (hole) concentration on *FF*, η, $V_{oc,}$ and J_{sc}. The η increased from 16.00% to 18.74% as the hole concentration (N_A) increased from 1×10^{13} cm^{-3} to 1×10^{17} cm^{-3}. Subsequently, the η reduces to 6.44% at a hole concentration of 1×10^{21} cm^{-3}. The increase of hole density (Δn) improves the carrier lifetime, as expressed in Eq. (11).

$$L = \sqrt{D\frac{\Delta n}{R}}, \tag{11}$$

where L is the diffusion length; $\frac{\Delta n}{R}$ is the minority carrier life, R is the recombination rate, and D is the diffusivity. The increment of carrier lifetime increased the diffusion length, L. It contributed higher carrier collection rate at the *p*- and *n*- terminals. The η of the solar cell

reduced significantly when the hole concentration was more than 1×10^{18} cm^{-3}. This anomaly was due to increasing surface recombination velocity in the less passivated absorber layer at a higher doping concentration, subsequently reducing the radiative recombination [37]. The reduction of J_{sc} was due to the reduction of radiative recombination, while the improvement of V_{oc} across the N_A can be explained by the separation of the quasi-Fermi level by Zhao *et al*. [38] in Eq. (12).

$$V_{oc} = \frac{kT}{q} ln\left(\frac{\Delta n}{N} + \frac{\Delta n^2}{n_i^2} + \frac{N\Delta n}{n_i^2} + 1\right), \quad (12)$$

where N is the doping concentration at equilibrium, Δn is the excess carrier concentration, and n_i is the intrinsic carrier concentration. Hence, the excess carrier concentration contributed to higher V_{oc}. This relation applies to the doping concentration of *i*- and *n*-layers as well. In terms of hole concentration, the optimized N_A is 1×10^{17} cm^{-3} with the *FF* of 90.56%, the η of 18.74%, V_{oc} of 1.45 V, and J_{sc} of 14.22 mA/cm^2.

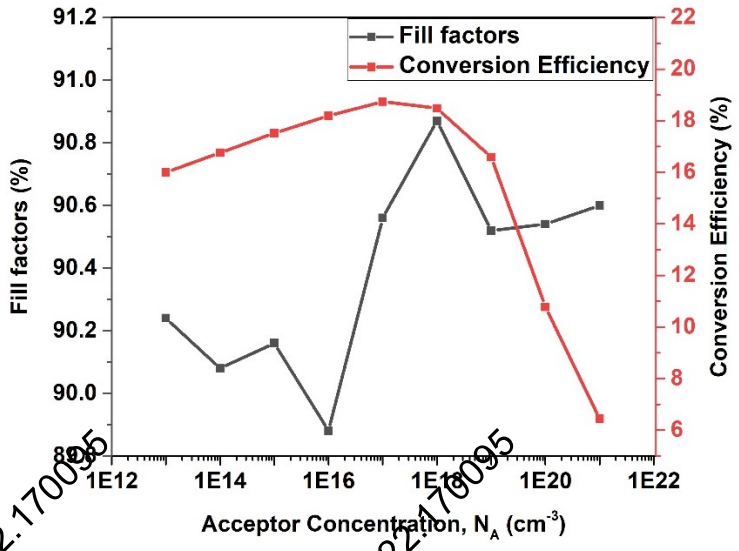

(a)

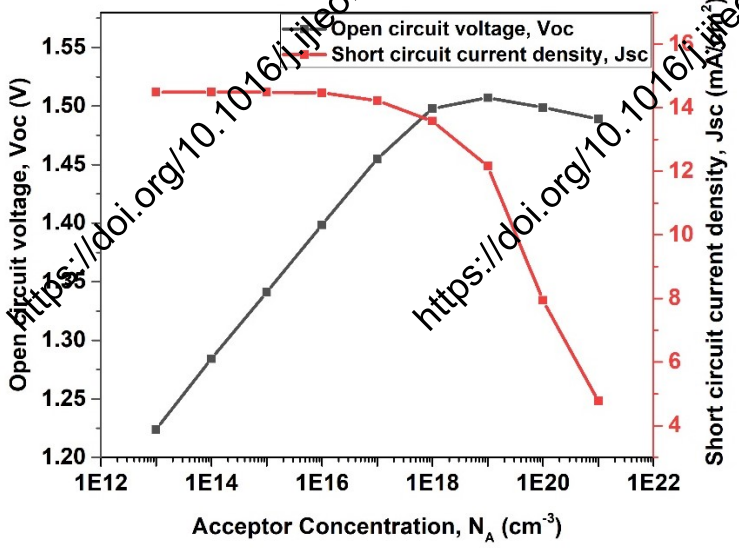

(b)

Figure 5. Effects of absorber's carrier density (N_A) on (a) fill factors and conversion efficiency, (b) open circuit voltage and short circuit current density of *p-i-n* InGaN-based solar cell.

The optimized N_A of 1×10^{17} cm^{-3} for the absorber was used to optimize the *i*- and *n*-layers. As the carrier concentration in the *i*-layer increased, *FF* and η remained constant at 90.57% and 18.74%, respectively, until the carrier concentration reached 1×10^{16} cm^{-3}, as shown in Figure 6(a). As the carrier concentration of the *i*-layer exceeded 1×10^{16} cm^{-3}, *FF* and η started to reduce. The behavior of V_{oc} and J_{sc} in Figure 6(b) was similar to the absorber layer due to

the excess carrier concentration. The reduction of the η from 18.74% to 18.54% at higher carrier concentration was due to the changes in quasi-Fermi level and the band energy between *p*-$In_{0.4}Ga_{0.6}N$/ *i*-$In_{0.4}Ga_{0.6}N$ and *i*-$In_{0.4}Ga_{0.6}N$/ *n*-$In_{0.4}Ga_{0.6}N$ interfaces.

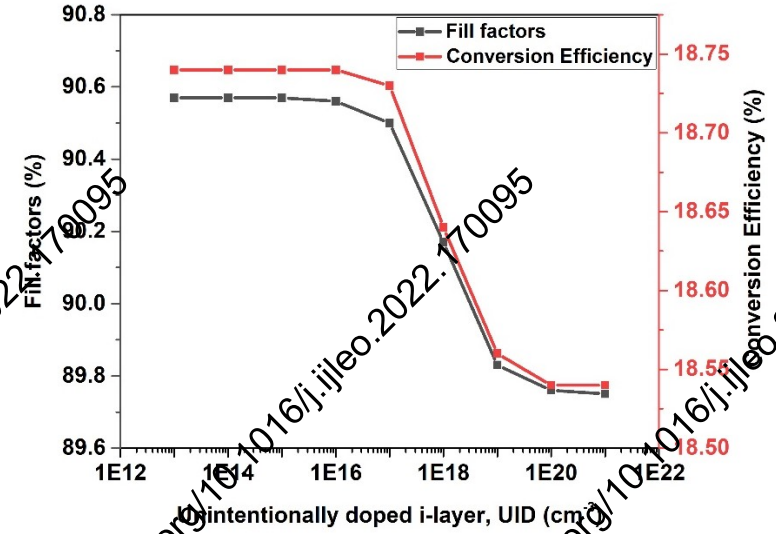

(a)

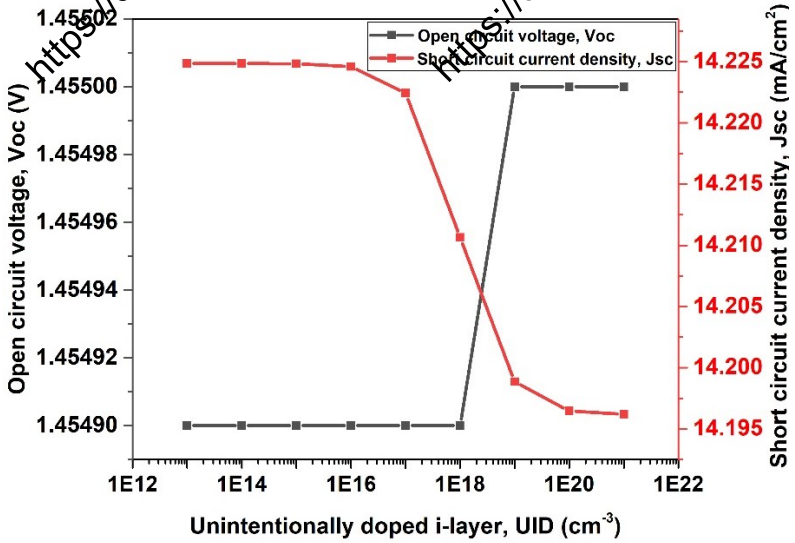

(b)

Figure 6. Effects of layer carrier density on (a) fill factors and conversion efficiency, (b) open circuit voltage and short circuit current density of *p-i-n* InGaN-based solar cell.

Figures 7(a) and 7(b) show the band diagrams of the standard *p-i-n* structure with two different carrier concentrations. The band energy difference of quasi-Fermi of holes (F_p) and

valence band (E_v) for *i*-layer with carrier concentration of 1×10^{19} cm^{-3} is much greater than 1×10^{16} cm^{-3}. The valence band offset (VBO) with the carrier concentration of 1×10^{16} cm^{-3} is 2.06 eV, which is much lower than 4.12 eV from the carrier concentration of 1×10^{19} cm^{-3}. Hence, the holes require more energy for recombination. Therefore, the η of the standard *p-i-n* solar cell reduces with *i*-layer carrier concentration.

The effects of electron concentration (N_D) on the electrical properties of the solar cell are shown in Figures 8(a) and 8(b). As the N_D increases, the η increases from 15.78% to 18.74%. Beyond the carrier concentration of 1×10^{17} cm^{-3}, the η shows a slight reduction from 18.74% to 18.67%. The behavior of the J_{sc} and V_{oc} is similar to the effect of doping concentration on *p*- and *i*-layers. Therefore, it can be concluded that the carrier density has almost no significant effect on the FF and η of the solar cell after the N_D exceeds 1×10^{17} cm^{-3}. In brief, the optimized results are summarized in Table 3.

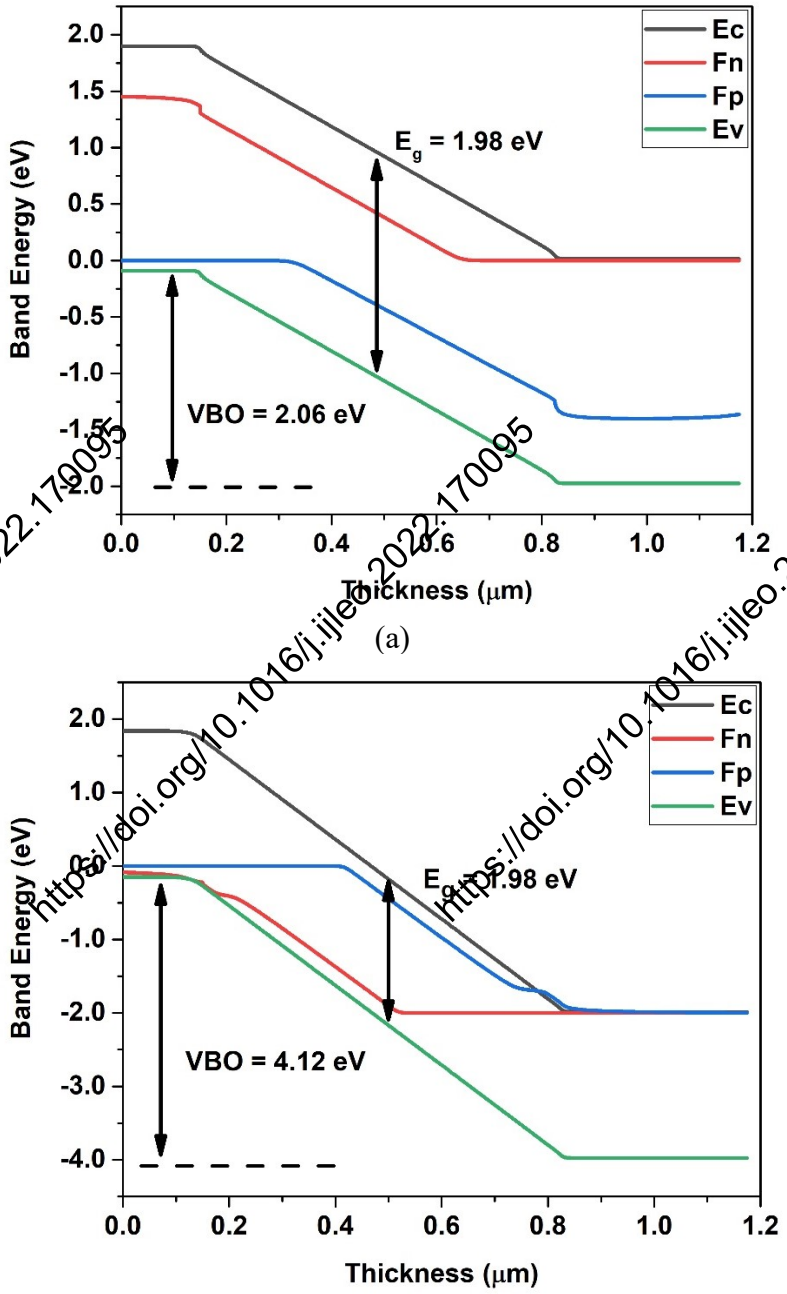

Figure 7. Band diagrams of *p-i-n* InGaN-based solar cell with different intrinsic layer carrier concentrations (a) 1×10^{16} cm^{-3} and (b) 1×10^{19} cm^{-3}.

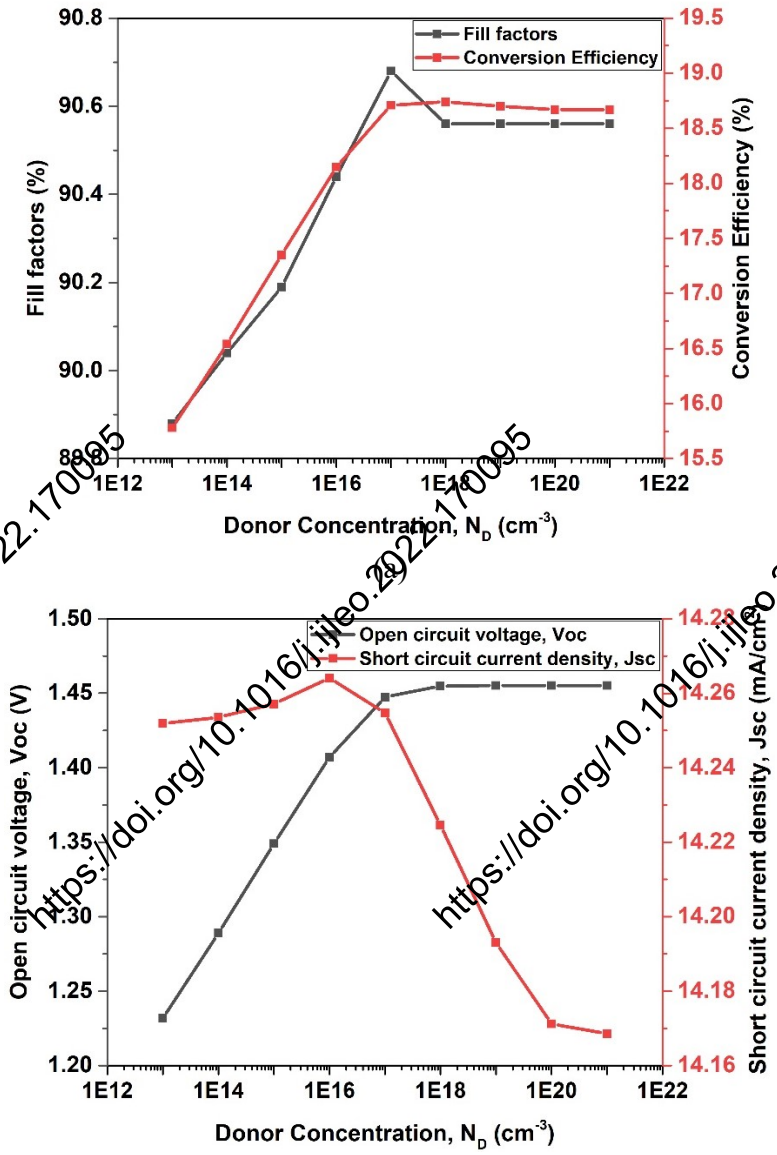

Figure 8. Effects of *n*-layer carrier density on (a) fill factors and conversion efficiency, (b) open circuit voltage and short circuit current density of *p-i-n* InGaN-based solar cell.

3.2 Effects of absorber design on the performance of solar cells.

This section proposed solar cells with graded bandgap absorbers to enhance the photon harness effectiveness at the absorber layer. The graded absorber layers were proposed to avoid abrupt changes to the energy bandgap in the solar cell structure as well as to reduce the lattice mismatch between GaN and InGaN. Therefore, the strain-induced piezoelectric and

spontaneous polarization can be reduced to improve the carrier collection [22]. The optimized parameters for the standard *p-i-n* structure shown in Table 3 were used as the reference for the absorber layer. For the linear-graded absorber, the absorber layer was changed to the $In_xGa_{1-x}N$ layer with a linear increment of In composition from 0% (GaN) on top to 40% ($In_{0.4}Ga_{0.6}N$) at the bottom of the absorber layer. The wider bandgap was placed on top to capture photons with higher bandgap energy into the intrinsic (*i*) layer, reducing the thermalization of "hot carriers" at higher bandgap energy, and improving the electron-hole generation and collection due to transferring kinetic energy in the electron via band-to-band impact ionization [39].

Table 3. Optimized results for the standard *p-i-n* InGaN solar cell.

Structural parameters	Values
p-layer initial thickness	150 nm
i-layer initial thickness	675 nm
n-layer initial thickness	350 nm
Acceptor doping density in *p*-layer, N_A	1×10^{17} cm^{-3}
Carrier density of intrinsic layer, N_i	1×10^{16} cm^{-3}
Donor doping density in *n*-layer, N_D	1×10^{18} cm^{-3}
Open circuit voltage, V_{oc}	1.45 V
Short-circuit current density, J_{sc}	14.22 mA/cm^2
Conversion efficiency, η	18.74%
Fill factor, *FF*	90.56%

Moreover, the linear-graded absorber was proposed in such a way as to enhance strain relaxation so that the effect of piezoelectric polarization was insignificant to the performance of the solar cell [11]. Song *et al.* (2003) investigated the In grading rate. They found that a higher grading rate will introduce more dislocations into the thin film. Eventually, the probability of dislocation entanglement will increase to impede the lattice relaxation process [40]. Therefore, the step-graded absorber *p-n* was introduced to prevent the possibility of a defect from the different In grading rates. The step-graded absorber *p-n* has one layer of GaN and 4 layers of $In_xGa_{1-x}N$ layers with each layer of 30 nm. The GaN layer on top of the step-

graded acts as the wide bandgap energy collector as well as the GaN cap to protect InGaN from In desorption during the annealing process. The growth of thick In-rich InGaN thin film is always associated with large 3D-island InN on the growing surface due to Stranski-Krastanov (SK) growth mode [41]. Therefore, a dual temperature GaN cap growth method helps dissolve In-rich 3D-island, spreading InN across the GaN surface more uniformly across the growing surface [42] and preventing In desorbing from the InGaN layer [43]. The step-graded absorber with 10% In increment for each layer helps reduce the lattice mismatch between the subsequent layers. It is relatively easier to grow by the MOCVD technique. The band diagrams of different absorber configurations are shown in Figure 9. Linear-graded absorber *p-i-n* shows a smooth reduction of bandgap energy from 3.42 eV (GaN) to 1.99 eV ($In_{0.4}Ga_{0.6}N$). In contrast, the step-graded absorber *p-i-n* shows a step-wise reduction of bandgap energy. The maximum QE reachable by linear- and step-graded absorber *p-i-n* structures are close to 100%. In comparison, the standard *p-i-n* structure can only reach a maximum QE of 95%, as shown in Figure 10. The linear- and step-graded absorber *p-i-n* structures improve the V_{oc}, J_{sc}, and η compared to standard *p-i-n* structures, as shown in Table 4. The performance of linear-graded absorber *p-i-n* was also found to be superior to step-graded absorber *p-i-n*. This is mainly attributed to the lesser abrupt bandgap energy changes during the band-to-band and inter-band absorption and lesser thermalization of energy across the absorber layer through the emission of phonon due to barrier height differences. Throughout this study, the best performance was achieved by linear-graded absorber *p-i-n* structure with *FF*, η, J_{sc}, and V_{oc} of 90.33%, 19.84%, 14.48 mA/cm^2, and 1.52 V, respectively.

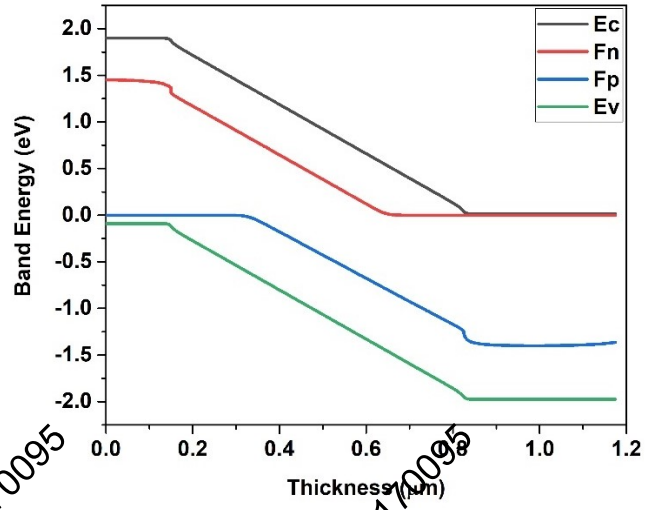

(a)

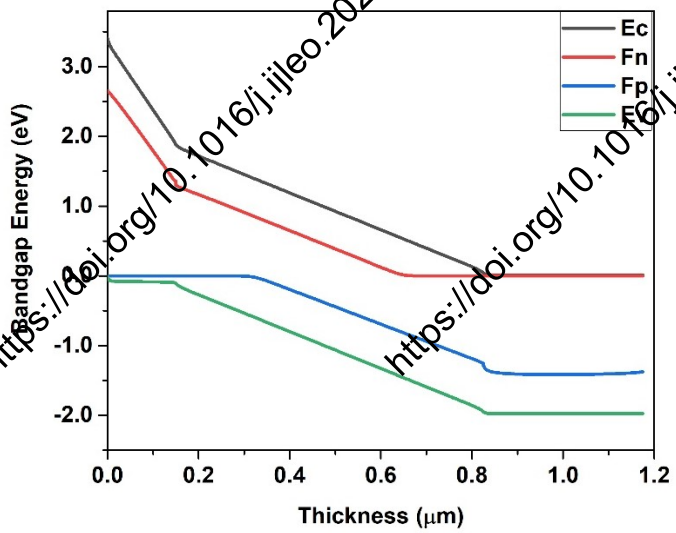

(b)

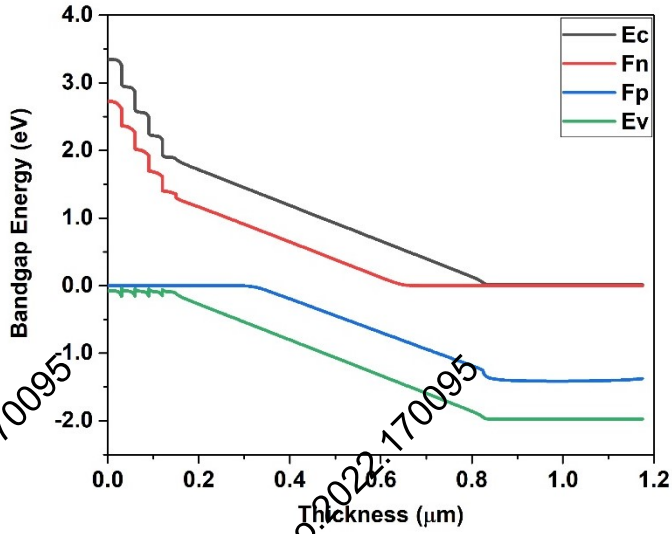

(c)

Figure 9. Band diagrams of (a) standard, (b) linear-graded absorber, and (c) step-graded absorber *p-i-n* InGaN-based solar cells.

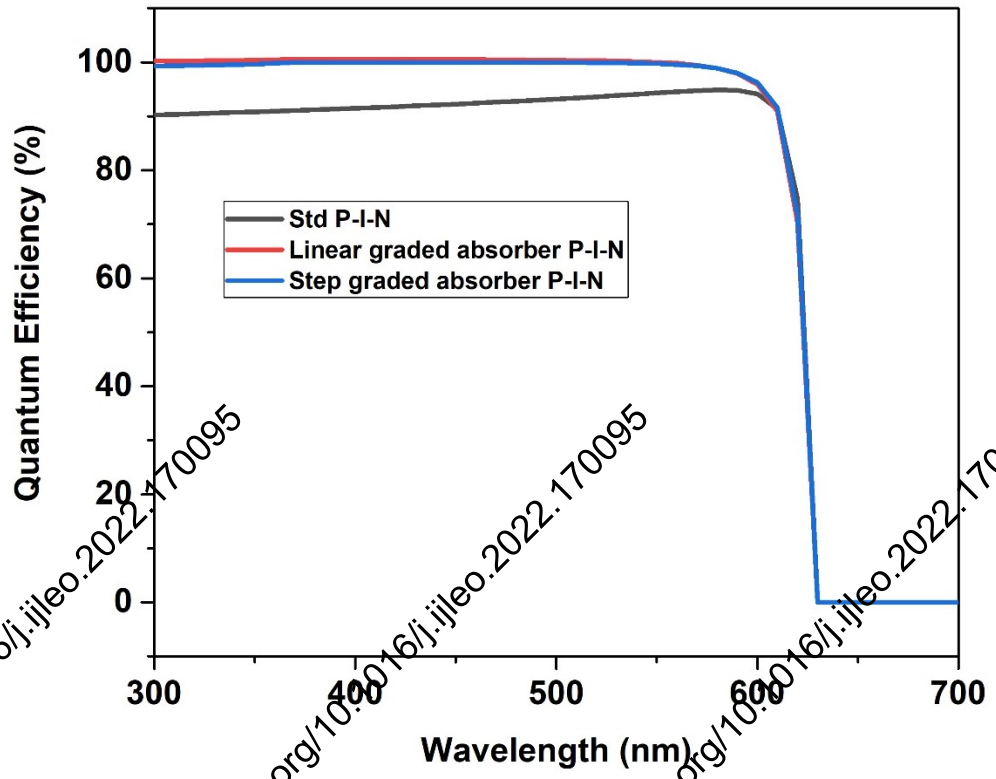

Figure 10. Comparison of quantum efficiency of *p-i-n* InGaN-based solar cells with different absorber configurations

Table 4. Performance of solar cells with different absorber configurations.

Solar cell configuration	Standard *p-i-n*	Linear-graded absorber *p-i-n*	Step-graded absorber *p-i-n*
Open-circuit voltage, V_{oc} (V)	1.45	1.52	1.52
Short-circuit current density, J_{sc} (mA/cm^2)	14.22	14.48	14.43
Conversion efficiency, η (%)	18.74	19.84	19.77
Fill Factor, *FF* (%)	90.56	90.33	90.34

4.0 Conclusion

In this study, optimization of intermediate In composition homojunction $In_{0.4}Ga_{0.6}N$ solar cell with *p-i-n* structure was performed by varying thicknesses, carrier concentration, and absorber configurations. The results revealed that the absorber thickness and the hole concentration have profound effects on the solar cell's performance. The graded absorber layer was also proposed to improve solar cell performance. The results showed that the linear- and step-graded absorbers have better conversion efficiency and exhibit QE close to 100% compared to the standard structure. The results also revealed that the performance of the linear-graded absorber was better than the step-graded absorber due to the lesser abrupt bandgap energy changes and lesser thermalization of energy across the absorber layer. In summary, these results implied the potential of intermediate In composition $In_{0.4}Ga_{0.6}N$. The implementation of graded In composition absorber configurations opens a new path for the growth and fabrication of InGaN-based solar cells such as single junction and tandem solar cells.

Authorship contribution statement

A.K. Tan: Writing – original draft, conceptualization, and formal analysis. H.U. Manzoor: Conceptualization and software. S.S. Ng: Project administrator, review and editing, supervision, funding acquisition. N.A. Hamzah: Review and editing. M.A. Ahmad: Review and editing. Z. Hassan: Review and editing.

Acknowledgments

This research was funded by Universiti Sains Malaysia, Malaysia, through the Research University Individual (RUI) Grant (Account No.: 1001/CINOR/8011127). The authors would like to thank Prof. Marc Rürgelman for his assistance in the development of the SCAPS-1D software and for providing technical consultation on using the software.

References

[1] N.A. Ludin, A.M. Al-Alwani Mahmoud, A. Bakar Mohamad, A.A.H. Kadhum, K. Sopian, N.S. Abdul Karim, Review on the development of natural dye photosensitizer for dye-sensitized solar cells, Renewable and Sustainable Energy Reviews. 31 (2014) 386–396. https://doi.org/10.1016/j.rser.2013.12.001.

[2] B.R. Bennett, R.A. Soref, J.A. Del Alamo, Carrier-Induced Change in Refractive Index of InP, GaAs and InGaAsP, IEEE Journal of Quantum Electronics. 26 (1990) 113–122. https://doi.org/10.1109/3.44924.

[3] A. ur Rehman, S.H. Lee, S.H. Lee, Silicon space solar cells: progression and radiation-resistance analysis, Journal of the Korean Physical Society. 68 (2016) 593–598. https://doi.org/10.3938/jkps.68.593.

[4] M.K. Hossain, M.T. Rahman, M.K. Basher, M.S. Manir, M.S. Bashar, Influence of thickness variation of gamma-irradiated DSSC photoanodic TiO2 film on structural, morphological and optical properties, Optik. 178 (2019) 449–460. https://doi.org/10.1016/j.ijleo.2018.09.170.

[5] K. Prabakaran, M. Jayasakthi, S. Surender, S. Pradeep, S. Sanjay, R. Ramesh, M. Balaji, K. Baskar, Investigations on morphology, growth mode and indium incorporation in MOCVD grown InGaN/n-GaN heterostructures, Optik. 175 (2018) 154–162. https://doi.org/10.1016/j.ijleo.2018.08.134.

[6] Ž. Podlipskas, J. Jurkevičius, A. Kadys, M. Kolenda, V. Kovalevskij, D. Dobrovolskas, R. Aleksiejūnas, G. Tamulaitis, Extreme radiation resistance in InN, Journal of Alloys and Compounds. 789 (2019) 48–55. https://doi.org/10.1016/j.jallcom.2019.03.108.

[7] D. Pal, S. Das, Numerical simulation of GaN/InGaN p-i-n solar cells: Role of interlayers in promoting photovoltaic response, Optik. 221 (2020) 165403. https://doi.org/10.1016/j.ijleo.2020.165403.

[8] A. Mesrane, F. Rahmoune, A. Mahrane, A. Oulebsir, Design and simulation of InGaN p-n junction solar cell, International Journal of Photoenergy. 2015 (2015) 1–9. https://doi.org/10.1155/2015/594858.

[9] M.O. Moustafa, T. Alzoubi, Numerical Simulation of Single Junction InGaN Solar Cell by SCAPS, Key Engineering Materials. 821 (2019) 407–413. https://doi.org/10.4028/www.scientific.net/KEM.821.407.

[10] S. Hussain, M.T. Prodhan, M.M. Rahman, Simulation analysis to optimize the performance of homojunction p-i-n In0.7Ga0.3N solar cell, Semiconductor Physics, Quantum Electronics and Optoelectronics. 24 (2021) 192–199. https://doi.org/10.15407/spqeo24.02.192.

[11] A.K. Tan, N.A. Hamzah, M.A. Ahmad, S.S. Ng, Z. Hassan, Recent advances and challenges in the MOCVD growth of indium gallium nitride: A brief review, Materials Science in Semiconductor Processing. 143 (2022) 106545. https://doi.org/10.1016/j.mssp.2022.106545.

[12] G.B. Stringfellow, Microstructures produced during the epitaxial growth of InGaN alloys, Journal of Crystal Growth. 312 (2010) 735–749. https://doi.org/10.1016/j.jcrysgro.2009.12.018.

[13] R. Dahal, B. Pantha, J. Li, J.Y. Lin, H.X. Jiang, InGaN/GaN multiple quantum well solar cells with long operating wavelengths, Applied Physics Letters. 94 (2009) 63505.

https://doi.org/10.1063/1.3081123.

[14] M.R. Islam, M.R. Kaysir, M.J. Islam, A. Hashimoto, A. Yamamoto, MOVPE growth of $In_xGa_{1-x}N$ (x ~ 0.4) and fabrication of homo-junction solar cells, Journal of Materials Science & Technology. 29 (2013) 128–136. https://doi.org/10.1016/j.jmst.2012.12.005.

[15] Y. Guo, X.L. Liu, H.P. Song, A.L. Yang, X.Q. Xu, G.L. Zheng, H.Y. Wei, S.Y. Yang, Q.S. Zhu, Z.G. Wang, A study of indium incorporation in In-rich InGaN grown by MOVPE, Applied Surface Science. 256 (2010) 3352–3356. https://doi.org/10.1016/j.apsusc.2009.11.081.

[16] L. Sang, M. Liao, M. Sumiya, X. Yang, B. Shen, High-pressure MOCVD growth of InGaN thick films toward the photovoltaic applications, Fundamental Research. (2021). https://doi.org/10.1016/j.fmre.2021.11.024.

[17] K. Kumakura, T. Makimoto, N. Kobayashi, High hole concentrations in Mg-doped InGaN grown by MOVPE, Journal of Crystal Growth. 221 (2000) 267–270. https://doi.org/10.1016/S0022-0248(00)00697-7.

[18] J.W.L. Yim, R.E. Jones, K.M. Yu, J.W. Ager, W. Walukiewicz, W.J. Schaff, J. Wu, Effects of surface states on electrical characteristics of InN and $In_{1-x}Ga_xN$, Physical Review B - Condensed Matter and Materials Physics. 76 (2007) 1–4. https://doi.org/10.1103/PhysRevB.76.041303.

[19] K. Sasamoto, T. Hotta, K. Sugita, A.G. Bhuiyan, A. Hashimoto, A. Yamamoto, K. Kuboshita, Y. Kohji, MOVPE growth of high quality p-type InGaN with intermediate in compositions, Journal of Crystal Growth. 318 (2011) 492–495.

https://doi.org/10.1016/j.jcrysgro.2010.10.217.

[20] B.N. Pantha, A. Sedhain, J. Li, J.Y. Lin, H.X. Jiang, Electrical and optical properties of p-type InGaN, Applied Physics Letters. 95 (2009) 10–13. https://doi.org/10.1063/1.3279149.

[21] C.A. Chang, T.Y. Tang, P.H. Chang, N.C. Chen, C. Te Liang, Magnesium doping of In-rich InGaN, Japanese Journal of Applied Physics, Part 1: Regular Papers and Short Notes and Review Papers. 46 (2007) 2840–2843. https://doi.org/10.1143/JJAP.46.2840.

[22] J.J. Wierer, A.J. Fischer, D.D. Koleske, The impact of piezoelectric polarization and nonradiative recombination on the performance of (0001) face GaN/InGaN photovoltaic devices, Applied Physics Letters. 96 (2010) 1–4. https://doi.org/10.1063/1.3301262.

[23] X.M. Cai, S.W. Zeng, B.P. Zhang, Fabrication and characterization of InGaN *p-i-n* homojunction solar cell, Applied Physics Letters. 95 (2009) 1–4. https://doi.org/10.1063/1.3254215.

[24] M.-T. Chu, W.-Y. Liao, M.-H. Wu, R.-H. Horng, T.-Y. Tsai, S.-P. Liu, Growth and Characterization of *p*-InGaN/*i*-InGaN/*n*-GaN Double Heterojunction Solar Cell on Patterned Sapphire Substrates, ECS Transactions. 35 (2011) 47–51. https://doi.org/10.1149/1.3570845.

[25] Y. Xing, D. Zhao, D. Jiang, Z. Liu, J. Zhu, P. Chen, J. Yang, W. Liu, F. Liang, S. Liu, L. Zhang, W. Wang, M. Li, Y. Zhang, G. Du, The role of temperature ramp-up time before barrier layer growth in optical and structural properties of InGaN/GaN multi-

quantum wells, Superlattices and Microstructures. 117 (2018) 228–234. https://doi.org/10.1016/j.spmi.2018.03.033.

[26] N. Ma, X.Q. Wang, S.T. Liu, G. Chen, J.H. Pan, L. Feng, F.J. Xu, N. Tang, B. Shen, Hole mobility in wurtzite InN, Applied Physics Letters. 98 (2011) 18–21. https://doi.org/10.1063/1.3592257.

[27] T.T. Mnatsakanov, M.E. Levinshtein, L.I. Pomortseva, S.N. Yurkov, G.S. Simin, M.A. Khan, Carrier mobility model for GaN, Solid-State Electronics. 47 (2003) 111–115. https://doi.org/10.1016/S0038-1101(02)00256-3.

[28] H.U. Manzoor, M.A.M. Zawawi, M.Z. Pakhuruddin, S.S. Ng, Z. Hassan, High conversion and quantum efficiency indium-rich *p*-InGaN/*p*-InGaN/*n*-InGaN solar cell, Physica B: Condensed Matter. 622 (2021) 413339. https://doi.org/10.1016/j.physb.2021.413339.

[29] R. Kour, S. Arya, S. Verma, A. Singh, P. Mahajan, A. Khosla, Review—recent advances and challenges in indium gallium nitride ($In_xGa_{1-x}N$) materials for solid state lighting, ECS Journal of Solid State Science and Technology. 9 (2020) 015011. https://doi.org/10.1149/2.0292001jss.

[30] Z. Xing, W. Yang, Z. Yuan, X. Li, Y. Wu, J. Long, S. Jin, Y. Zhao, T. Liu, L. Bian, S. Lu, M. Luo, Growth and Characterization of High In-content InGaN grown by MBE using Metal Modulated Epitaxy Technique (MME), Journal of Crystal Growth. 516 (2019) 57–62. https://doi.org/10.1016/j.jcrysgro.2019.03.021.

[31] K. Prabakaran, R. Ramesh, P. Arivazhagan, M. Jayasakthi, S. Sanjay, S. Surender, S. Pradeep, M. Balaji, K. Baskar, Effects of indium flow rate on the structural,

morphological, optical and electrical properties of InGaN layers grown by metal organic chemical vapour deposition, Journal of Alloys and Compounds. 811 (2019) 151803. https://doi.org/10.1016/j.jallcom.2019.151803.

[32] J. Meyer, R. Liu, R.D. Schaller, H.P. Lee, C. Bayram, Systematic study of shockley-read-hall and radiative recombination in GaN on Al_2O_3, freestanding GaN, and GaN on Si, Journal of Physics: Photonics. 2 (2020). https://doi.org/10.1088/2515-7647/ab9072.

[33] A. V. Sinovchuk, A.M. Gryschuk, Alloy-assisted Auger recombination in InGaN, Optical and Quantum Electronics. 50 (2018) 455. https://doi.org/10.1007/s11082-018-1704-9.

[34] T. Ouslimane, L. Et-taya, L. Elmaimouni, A. Benami, Impact of absorber layer thickness, defect density, and operating temperature on the performance of $MAPbI_3$ solar cells based on ZnO electron transporting material, Heliyon. 7 (2021) e06379. https://doi.org/10.1016/j.heliyon.2021.e06379.

[35] I. Benigno, D. Darminto, Effect of Intrinsic Layer Energy Gap and Thicknesses Optimization on the Efficiency of *p-i-n* Amorphous Silicon Solar Cell, IPTEK Journal of Science. 2 (2017). https://doi.org/10.12962/j23378530.v2i3.a3184.

[36] C.A.M. Fabien, W.A. Doolittle, Guidelines and limitations for the design of high-efficiency InGaN single-junction solar cells, Solar Energy Materials and Solar Cells. 130 (2014) 354–363. https://doi.org/10.1016/j.solmat.2014.07.018.

[37] A.K. Das, Efficiency improvement of *p-i-n* structure over *p-n* structure and effect of *p*-layer and *i*-layer properties on electrical measurements of gallium nitride and indium

nitride alloy based thin film solar cell using AMPS -1D, IOSR Journal of Applied Physics. 7 (2015) 8–15. https://doi.org/10.9790/4861-07220815.

[38] Y. Zhao, C. Liang, M. Sun, Q. Liu, F. Zhang, D. Li, Z. He, Effect of doping on the short-circuit current and open-circuit voltage of polymer solar cells, Journal of Applied Physics. 116 (2014). https://doi.org/10.1063/1.4898692.

[39] A.A. Ojo, W.M. Granton, I.M. Dharmadasa, Next Generation Multilayer Graded Bandgap Solar Cells, Springer International Publishing, Cham, 2019. https://doi.org/10.1007/978-3-319-96667-0.

[40] T.L. Song, S.J. Chua, E.A. Fitzgerald, P. Chen, S. Tripathy, Strain relaxation in graded InGaN/GaN epilayers grown on sapphire, Applied Physics Letters. 83 (2003) 1545–1547. https://doi.org/10.1063/1.1598295.

[41] A. Kadys, T. Malinauskas, T. Grinys, M. Dmukauskas, J. Mickevičius, J. Aleknavičius, R. Tomašiūnas, A. Selskis, R. Kondrotas, S. Stanionytė, H.-J. Lugauer, M. Straßburg, M. Strassburg, Growth of InN and In-Rich InGaN Layers on GaN Templates by Pulsed Metalorganic Chemical Vapor Deposition, Journal of Electronic Materials. 44 (2015) 188–193. https://doi.org/10.1007/s11664-014-3494-6.

[42] C. Tessarek, S. Figge, T. Aschenbrenner, S. Bley, A. Rosenauer, M. Seyfried, J. Kalden, K. Sebald, J. Gutowski, D. Hommel, Strong phase separation of strained InxGa1-xN layers due to spinodal and binodal decomposition: formation of stable quantum dots, Physical Review B. 83 (2011) 115316. https://doi.org/10.1103/PhysRevB.83.115316.

[43] J. Yang, D.G. Zhao, D.S. Jiang, P. Chen, J.J. Zhu, Z.S. Liu, L.C. Le, X.G. He, X.J. Li,

H. Yang, Y.T. Zhang, G.T. Du, Photovoltaic response of InGaN/GaN multi-quantum well solar cells enhanced by inserting thin GaN cap layers, Journal of Alloys and Compounds. 635 (2015) 82–86. https://doi.org/10.1016/j.jallcom.2015.02.052.

[44] L.-W. Feng, Shih-Wei and Lai, Chih-Ming and Tsai, Chin-Yi and Su, Yu-Ru and Tu, S.-W. Feng, C.-M. Lai, C.-Y. Tsai, Y.-R. Su, L.-W. Tu, Modeling of InGaN p-n junction solar cells, Optical Materials Express. 3 (2013) 1777. https://doi.org/10.1364/OME.3.001777.

[45] S.-W. Feng, C.-M. Lai, C.-H. Chen, W.-C. Sun, L.-W. Tu, Theoretical simulations of the effects of the indium content, thickness, and defect density of the *i*-layer on the performance of p-i-n InGaN single homojunction solar cells, Journal of Applied Physics. 108 (2010) 093118. https://doi.org/10.1063/1.3484040.

[46] N. Akter, Design of a Highly Efficient InGaN Single Junction Solar Cell Designed from Numerical Analysis, International Journal for Research in Applied Science and Engineering Technology. 6 (2018) 2614–2618. https://doi.org/10.22214/ijraset.2018.3585.